Journal of
Materials Chemistry A

ROYAL SOCIETY
OF CHEMISTRY

PAPER

View Article Online
View Journal

Check for updates

Cite this: DOI: 10.1039/d0ta09211h

Oxide nanomembrane induced assembly of a functional smart fiber composite with nanoporosity for an ultra-sensitive flexible glucose sensor†

Zhe Zhao,[a] Ye Kong,[a] Xinyi Lin,[a] Chang Liu,[a] Jinrun Liu,[a] Yiyun He,[b] Lili Yang,[b]
Gaoshan Huang *[a] and Yongfeng Mei *[a]

Received 19th September 2020
Accepted 23rd November 2020

DOI: 10.1039/d0ta09211h

rsc.li/materials-a

Smart cloth, as well as smart fibers, exhibits promising prospects in wearable electronics applications. However, very few kinds of smart fibers can be applied in the biomedical-related area, and the high cost and the poor adhesion between the functional layer and textile substrate remain challenging. Here, we present an efficient strategy utilizing atomic layer deposition pretreatment to induce the growth of hydroxy double salt (HDS) nanosheets on carbon fibers, and the HDS nanosheets are then chemically converted into a zeolitic imidazolate framework-67 layer, which closely attaches to the carbon fibers, forming composite Co-containing porous smart fibers (Co-PSF). On these smart fibers, a three-dimensional (3D) functional film is assembled and intimately adheres to the surface of the fibers, forming a hierarchical nanostructure with an enhanced surface area. The corresponding increased exposure of active sites and the improved electron transfer in the composite lead to improved efficiency of the electrochemical reaction and result in excellent glucose sensing in terms of good anti-interference ability, fast response, and an ultrahigh sensitivity of 4835 μA mM^{-1} cm^{-2}. Furthermore, the smart textile derived from Co-PSF shows good flexibility and stable electrochemical performance under 100 cycles of 180° bending.

1 Introduction

Glucose is considered an essential biological component existing in biology and food. For clinical purposes, the glucose concentration in body fluid is an important index for disease diagnosis.[1,2] For example, diabetes has become one of the major diseases threatening human health, and continuous glucose level monitoring of patients plays an important role in glycemic control.[3] Up to now, the evaluation of human glucose content has been based on the collection of blood, which causes pain and suffering to the body.[4] Recently, plenty of researchers have shown that the concentration of glucose in sweat is closely related to the glucose concentration in blood, and the sensing of glucose in sweat is quite promising.[5–7] However, more efforts are needed to improve the sensitivity, anti-interference, and convenience of sweat glucose sensors.[8–10] The electrochemical technique has become an ideal technique due to its high sensitivity, short analysis time, and easy operation.[11,12] In the initial studies concerning electrochemical detection of glucose, glucose oxide enzymes were applied on the device electrode.[13,14] Although the high efficiency of enzymatic biosensors makes for good selectivity, great biocompatibility, and good anti-interference properties of the device, natural enzymes are difficult to store, require high preparation cost and are vulnerable under environmental conditions, which limit their practical application and development.[15,16] Hence, designing convenient non-enzymatic biosensors has attracted a great deal of interest among researchers.

For non-enzymatic biosensors, efficient functional contents of the electrode are the most important part. We observed that metal organic frameworks (MOFs) are a series of porous materials composed of metal ions with organic bridging ligands and have drawn tremendous attention in a large variety of fields.[8,17–23] MOFs have shown great potential in non-enzymatic biosensing due to their large surface area, highly active sites, and high catalytic transition metal content.[10,24,25] Plenty of research has been devoted to fabricating MOF based electrodes applied in non-enzymatic biosensors.[26–29] For instance, Yamauchi *et al.*[26] presented a general method to synthesize benzene dicarboxylic acid-based MOFs with hierarchical 3D morphologies applied in glucose sensors. The

---

[a] *Department of Materials Science, Fudan University, Shanghai 200433, P. R. China. E-mail: gshuang@fudan.edu.cn; yfm@fudan.edu.cn*

[b] *State Key Laboratory for Modification of Chemical Fibers and Polymer Materials, College of Materials Science and Engineering, Donghua University, Shanghai 201620, P. R. China*

† Electronic supplementary information (ESI) available. See DOI: 10.1039/d0ta09211h

novel and stable structure exhibits outstanding sensing performance and has a great effect on MOF-based sensors. Generally, MOFs used for sensors are in the form of particles. However, the poor conductivity of MOFs hinders the release of catalytic ions and the lack of hierarchical nanostructures reduces the exposure of active sites, which may influence the performance of the sensing devices.[30–34] The configuration of individual rigid particles also limits the practical application of MOFs in devices.[35–37] The fabrication of a MOF layer on a conductive substrate could be an option to solve these problems. It was reported that the rapid self-nucleation of MOFs hinders the formation of a uniform layer on the substrate.[38] Up to now, plenty of researchers have concentrated on the integration of MOFs on substrates after nucleation,[39–41] while low mass loading of the MOF component and weak adhesion at the interface are noticeable.[38,39,42,43] The shape and the surface composition of the substrate also remarkably affect the structure of the resultant composites,[44] making the integration process uncontrollable. To handle these challenges, recently, we developed a new efficient strategy by utilizing atomic layer deposition (ALD) to induce the growth of a uniform MOF functional layer on flexible foam. The hierarchically porous structure and the firm adhesion between the functional layer and the substrate endow the composites with excellent electrochemical performance.[45,46] However, in order to fabricate such composites on versatile substrates, the mechanism of ALD-induced growth of the MOF film needs further investigation and the application of composites in bio-related sensing deserves further exploration.

Herein, by taking advantage of the conformal, uniform, and highly controllable deposition of the ALD technique, we fabricated a hydroxy double salt (HDS)-converted zeolitic imidazolate framework-67 (ZIF-67) layer on the surface of flexible carbon fibers (CFs) with the help of ALD induction. The composite (*i.e.*, ZIF-67 on CFs) was named Co-containing porous smart fiber (Co-PSF) and was used in a high-performance non-enzymatic glucose sensor. We specifically investigated the mechanism of ALD induced assembly of the functional layer with the help of detailed microstructural characterization. In the resultant smart fiber composite, the conductive CF substrate remarkably enhances the charge transportation. The surface assembly of the functional film preserves the original coordination structure and nanoporous structure of ZIF-67, which provide a large surface area and highly active sites simultaneously. Owing to its unique and stable structure, our smart fiber exhibits outstanding electrochemical performance in terms of ultrahigh sensitivities of 4835 μA mM^{-1} cm^{-2} at relatively low glucose concentrations of 0.0005–0.03 mM and 1055 μA mM^{-1} cm^{-2} in a linear range of 0.1–1 mM. The fast response of the device to variations of the glucose concentration guaranteed its real-time applications. Furthermore, due to the uniform coating and firm adhesion, the smart fiber and corresponding textile exhibit great flexibility, demonstrating stable performance under repeated and extreme bending conditions. Our work demonstrates a prototype of a glucose sensor on the skin, and its wide application can be expected.

2 Experimental section

2.1 Materials

The CFs used in the experiments were obtained from Toray, T-700 (Tokyo, Japan). Cobalt nitrate hexahydrate ($Co(NO_3)_2\cdot 6H_2O$), 2-methylimidazole (2-MI), and Nafion (5 wt%) were purchased from Aladdin Ltd (Shanghai, China). D-(+)-Glucose monohydrate (AR, ≥99.7%) and lactic acid (AR, ≥99.7%) were obtained from Sinopharm Chemicals. Dopamine hydrochloride (≥97%) and ascorbic acid (≥99.99%) were purchased from Aladdin Ltd (Shanghai, China). Methanol (AR, ≥99.5%) was obtained from Sinopharm Chemicals and ethanol (AR, ≥99.7%) was purchased from Titan Ltd. All the reagents were used as received without further purification. The DI water used throughout all the experiments was purified through a Millipore system.

2.2 ZnO nanomembrane deposited by ALD

A ZnO nanomembrane was deposited on CFs through ALD technology reported in our previous study.[46] The deposition of the ZnO nanomembrane on the exposed surface of CFs was performed at 150 °C in a homemade reactor. Diethylzinc (DEZ) and DI water were used as precursors. A typical ALD cycle included a DEZ pulse (50 ms), waiting time (5 s), a N_2 purge (30 s), a DI water pulse (30 ms), waiting time (5 s), and a N_2 purge (30 s). In the current study, the ZnO nanomembrane was deposited on CFs with 300 ALD cycles.

2.3 Fabrication of the ZIF-67 layer on CFs

$Co(NO_3)_2\cdot 6H_2O$ (1.45 g) was dissolved in a mixture of methanol (40 mL) and ethanol (40 mL) to form solution A. 2-MI (1.65 g) was dissolved in a mixture of methanol (40 mL) and ethanol (40 mL) to form solution B. ALD ZnO-coated CFs (CFs pretreated with 300 cycles of ALD of ZnO) were then placed in a beaker containing solution A. The beaker was sealed at 90 °C for 24 h. After cooling to room temperature (formation of HDS), solution B was added, and the mixture was aged at room temperature for another 24 h. After this, the fibers were taken out and washed with ethanol. The sample was subsequently dried in a vacuum at 60 °C for 12 h. This process led to the formation of a uniform ZIF-67 layer on the surface of CFs (see below) and the composite was named Co-PSF. In order to investigate the growth mechanism of the ZIF-67 layer, reference samples were prepared with different aging times and characterized with SEM.

2.4 Synthesis of the ZIF-67 powder

ZIF-67 powder was also synthesized for comparison. Solutions A and B were mixed with vigorous stirring for 5 min and then aged in a beaker at room temperature for 24 h. The product was centrifuged, washed with ethanol 3 times, and finally dried at 60 °C for 12 h in a vacuum.

2.5 Structural characterization

The morphologies of all the products were observed by field-emission scanning electron microscopy (SEM) using a VEGA TS 5136 MM (TESCAN Co., Czech). The X-ray diffraction (XRD) patterns were obtained using an X'Pert Pro X-ray diffractometer equipped with Cu Kα radiation ($\lambda = 0.1542$ nm) at a current of 40 mA and voltage of 40 kV. A Quadrasorb adsorption instrument (Quantachrome Instruments) was used to perform the nitrogen sorption/desorption measurements. The specific surface area was calculated using the single-point Brunauer–Emmett–Teller (BET) method. The pore size distributions were calculated from the nitrogen sorption data using the Barrett–Joyner–Halenda (BJH) method provided by Quantachrome data reduction software ASiQwin Version 4.01. The electrical properties of the samples were analyzed using a semiconductor parameter analyzer (Keithley 4200). Thermogravimetric analysis (TGA) was performed with an STA449F3 (NETZSCH, Germany) instrument in an air atmosphere with a heating rate of 10 °C min^{-1}. An energy dispersive spectrometer (EDS, Oxford X-Max 80T) was utilized to analyze the composition of the sample. X-ray photoelectron spectroscopy (XPS) analyses were performed with a VG ESCALAB 220I-XL device. Curve fitting for all the XPS spectra was accomplished by using XPS Peak 4.1 software.

2.6 Electrochemical characterization

The electrochemical glucose sensing tests were performed on a CHI 660E (Chenhua Instrument, Shanghai, China) with three-electrode configuration. In our experiment, Ag/AgCl (in saturated KCl solution) was used as the reference electrode and a graphite rod was used as the counter electrode. The working electrode was prepared by pasting the sample on glassy carbon (diameter: 5 mm) by using Nafion. For flexible property measurement, the smart textiles were directly used as the working electrode. The details of the electrochemical measurements can be found in the ESI.† For comparison, a ZIF-67 powder modified glassy carbon (GC, diameter: 5 mm) electrode was also used as the working electrode. Bare GC was first polished to a mirror finish successively using 1.0, 0.3, and 0.05 μm alumina slurry and then sonicated alternately in ethanol and deionized water several times. The active material was prepared by sonicating a mixture of 4.0 mg ZIF-67, 970 μL ethanol, and 30 μL Nafion (5 wt%) for 40 min. Next, 5 μL of the dispersion ink was dropped onto the well-polished GC electrode and then dried under ambient conditions.

3 Results and discussion

3.1 Characterization

Fig. 1a shows the schematic of the functional smart fiber and corresponding smart textile for high-performance glucose sensing, where a dense and uniform functional film is attached to the surface of the CF. As shown in Fig. 1c, the SEM image of Co-PSF at low magnification reveals rough structures wrapped over the surface of the CFs, indicating the growth of the functional film. For comparison, the SEM image of pristine CF is shown in Fig. 1b. Completely different morphologies can be observed and the regular cylindrical shape of the CFs makes for good mechanical properties.[47] In order to check the adhesion between the ZIF-67 layer and the CF, the Co-PSF was subjected to ultra-sonication treatment for 1 h. As shown in Fig. 1d, no

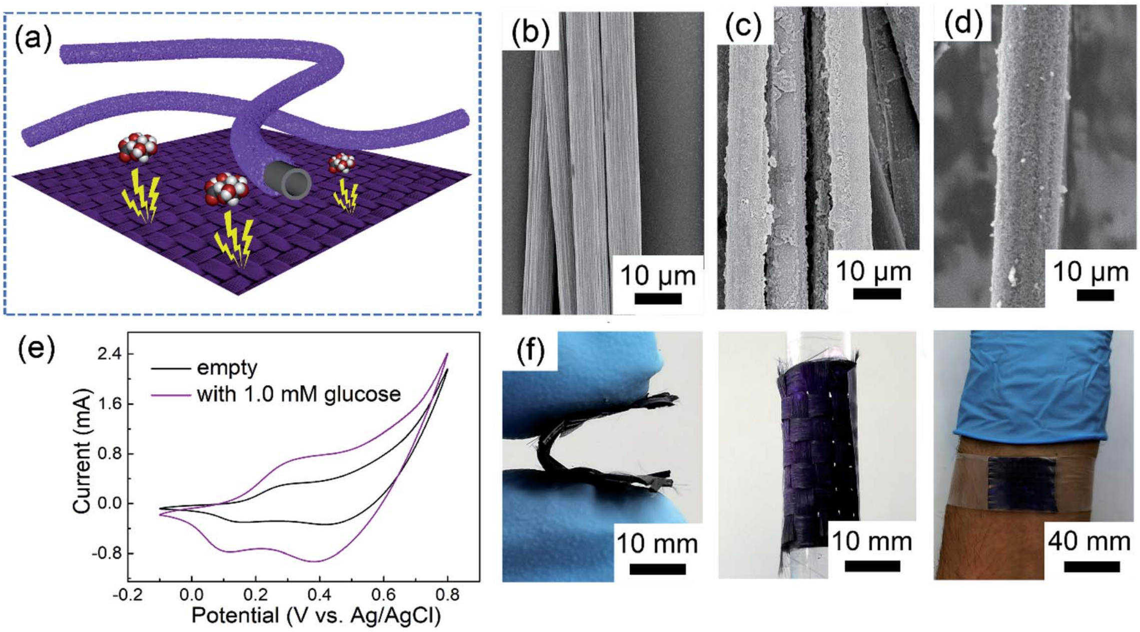

Fig. 1 (a) Schematic illustration of the functional smart fiber as well as the corresponding functional textile. (b) SEM image of pristine CFs at low magnification. (c) SEM image of Co-PSF at low magnification. (d) SEM image of Co-PSF after 1 h of ultra-sonication treatment at low magnification. (e) CV curves of the Co-PSF electrode with and without 1 mM glucose at a scan rate of 20 mV s^{-1}. (f) Photographs of the functional textile under bending and rolling conditions and adhered to human skin.

morphological changes can be observed, indicating an outstanding structural stability. Here as a preliminary demonstration, Fig. 1e shows the cyclic voltammetry (CV) scans of the Co-PSF electrode at a scan rate of 20 mV s^{-1} within the potential range of -0.1 to 0.8 V with and without 1 mM glucose in the electrolyte. Two reduction peaks at ~0.45 and ~0.13 V and one broad oxidation peak at ~0.3 V are noticeable. Attention should be paid to the fact that the current response of reduction and oxidation peaks is remarkably enhanced with 1 mM glucose, suggesting that Co-PSF is capable of catalyzing the oxidation of glucose to generate additional current. Taking advantage of the ALD technique, the coating of the functional film on the CFs is conformal,[48] and the corresponding firm adhesion produces a stable composite structure. The smart fiber could easily be woven into functional textiles, such as smart tattoo stickers, smart cloth, and other textiles that could adhere to skin. Fig. 1f exhibits typical photographs of our smart textile under bending and rolling conditions. The soft and flexible textile can closely adhere to human skin and maintain its mechanical properties as well as its glucose sensing performance under deformation, which will be specifically discussed later.

Here we further investigated the growth mechanism and the nucleation process of MOFs with the induction of the ALD ZnO nanomembrane. After ALD pretreatment for 300 cycles, a thin ZnO nanomembrane was deposited on the surface of the CF with a thickness of ~50 nm, and the sample was called ALD-ZnO-CF for short. Fig. 2a–i shows the schematic of ALD-ZnO-CF, while Fig. 2a(ii) and (iii) show the corresponding SEM images at low and high magnifications, respectively. Because of the uniform and conformal deposition, the morphology of ALD-ZnO-CF is similar to that of the pristine CF. As shown in Fig. 2b, after the introduction of cobaltous nitrate hexahydrate, 2D layered lamellar crystals emerge, implying the possible occurrence of phase transition. According to our previous research,[45,46] the ZnO nanomembrane reacted with cobaltous nitrate hexahydrate to form a (Zn, Co) hydroxy double salt (Zn, Co-HDS), which was attached to the surface of the substrate as an intermediate (*i.e.*, Zn, Co-HDS-CF). As shown in Fig. S1,† the thickness of the Zn, Co-HDS layer is ~200 nm. After this, when the organic linker (2-MI) was added, some Zn, Co-HDS reacted with 2-MI and a new phase (*i.e.*, MOF/HDS-CF) emerged (Fig. 2c). During this process, N^{3-} and NH^{2-} in 2-MI provided active electrons to break the crystal structure of HDS, and highly active NO^{3-} and OH^{-} in the HDS tended to cause rapid anion exchange. Therefore, with gradual exposure to 2-MI, the lamellar sheets began to collapse and NO^{3-} and OH^{-} were removed to release Co^{2+}, which coordinated *in situ* with [2-MI] continuously. This whole process led to the formation of target 3D particle-like crystals.[46,49] At this stage, the co-existence of the lamellar sheet and MOF crystals can be clearly seen (Fig. 2c(ii) and (iii)). After a full aging process, all the Zn, Co-HDS transformed into ZIF-67 and were assembled on the 3D surface of the CF. As shown in Fig. 2d(ii) and (iii), high quality assemblies of the MOF film consisting of dodecahedral particles can be observed on the surface of the CF. According to Fig. S2,† the thickness of the resultant MOF film is ~200 nm. We conclude that the whole induced assembly process should be based on the following two equations:

$$\begin{aligned}&Co(NO_3)_2\cdot 6H_2O + ZnO \rightarrow\\&\qquad (Zn,Co)_2(OH)_3NO_3 + (Zn,Co)_5(OH)_8(NO_3)_2\end{aligned} \tag{1}$$

$$\begin{aligned}&(Zn,Co)_2(OH)_3NO_3 + (Zn,Co)_5(OH)_8(NO_3)_2 + 2\text{-}MI \rightarrow\\&\qquad [Co(MI)_4]_n + Zn(NO_3)_2\end{aligned} \tag{2}$$

The reaction process provides abundant nucleation sites on substrates, which guides the growth of MOF crystals and prohibits the rapid self-nucleation of MOFs and aggregation of particles. This fact therefore explains the formation of the uniform MOF film and the firm adhesion at the interface. To confirm this advantage, we prepared ZIF-67 on CFs without the

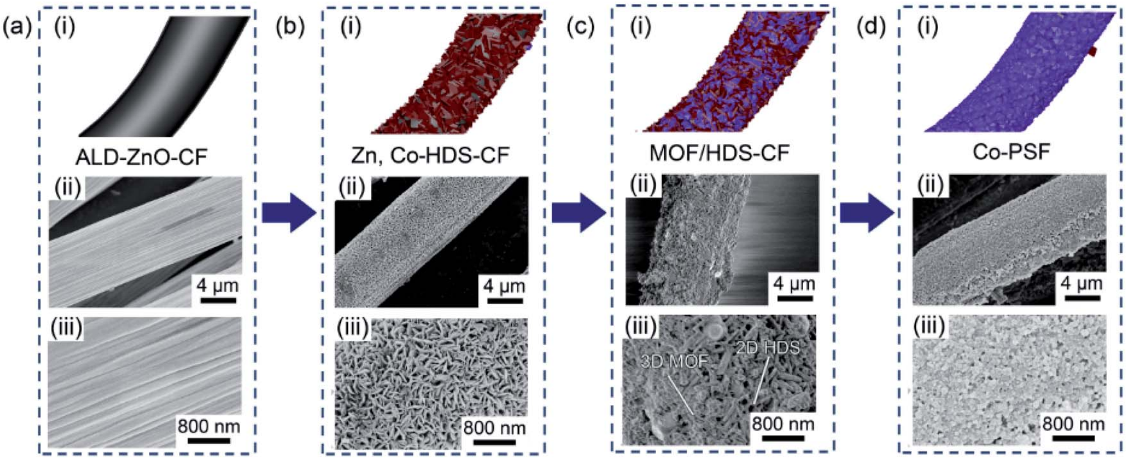

Fig. 2 Schematic illustrations of the growth process of Co-PSF. (a), (b), (c), and (d) represent ALD-ZnO-CF, Zn, Co-HDS-CF, MOF/HDS-CF, and Co-PSF, respectively. Panels (i), (ii), and (iii) are the corresponding scheme, SEM image at low magnification, and SEM image at high magnification, respectively. The process (a) to (b) is the growth of 2D lamellar crystals. The process (b) to (c) is the conversion from lamellar crystals to MOF crystals, and the process (c) to (d) is the aging process, which produces the Co-PSF.

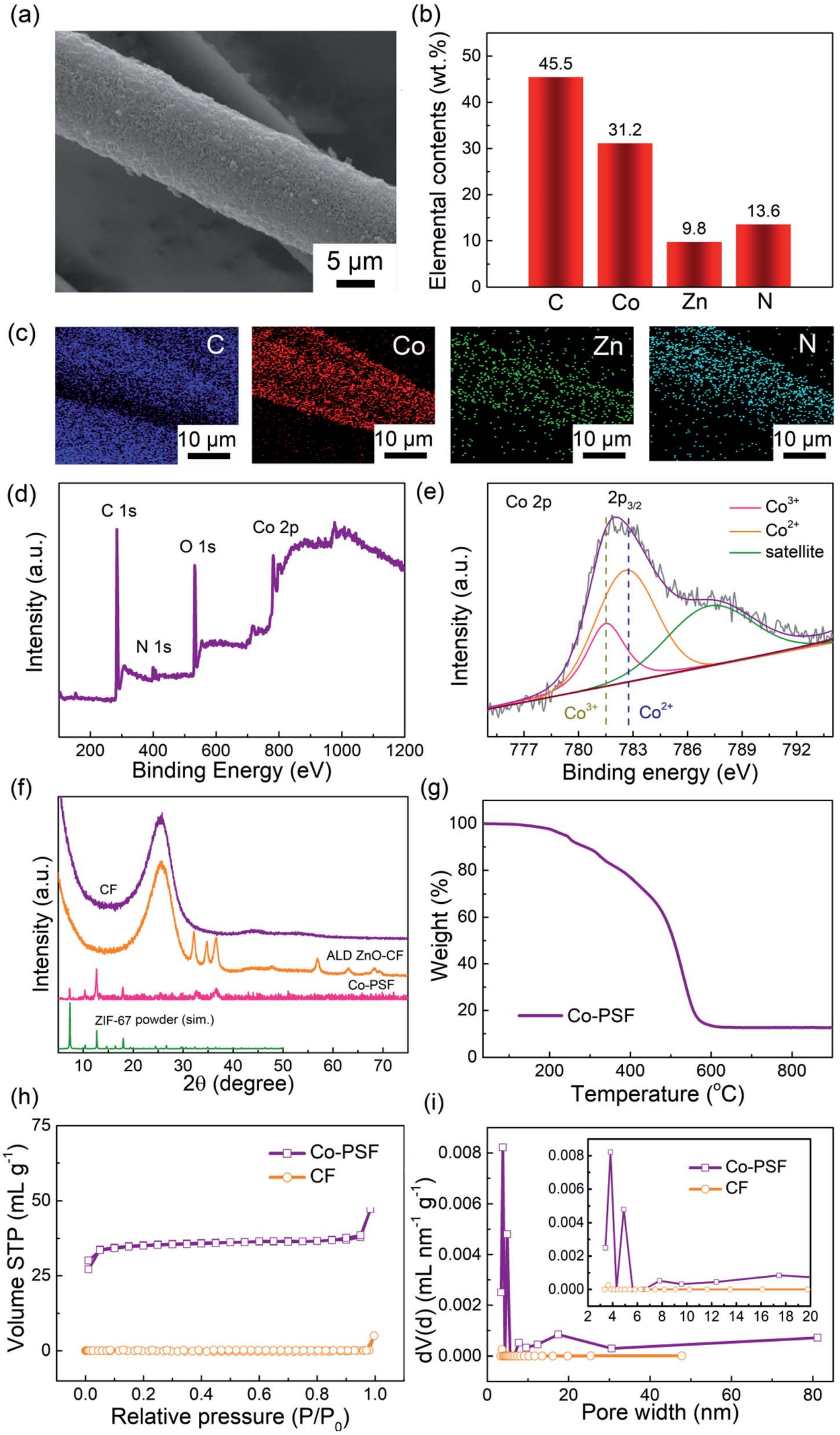

Fig. 3 (a) SEM image of Co-PSF. (b) Elemental contents of Co-PFS. (c) EDS mapping corresponding to (a), showing the presence of C, Co, N, and very little Zn. (d) XPS survey scan. (e) High resolution Co $2p_{3/2}$ spectrum. (f) XRD patterns of Co-PSF, pristine CFs, and ALD ZnO-CF. (g) TGA curve of obtained Co-PSF. (h) Nitrogen adsorption–desorption isotherms of Co-PSF and pristine CFs. (i) Corresponding pore size distributions of Co-PSF and pristine CFs. Part of the curves are enlarged in the inset of (i).

ALD ZnO nanomembrane for comparison. As shown in the Fig. S3,† low mass loading and incomplete wrapping were observed when no ZnO induction layer was adopted. Ultrasonication treatment for 1 h led to complete removal of the ZIF-67 particles (Fig. S3d†). The difference is ascribed to the fact that without the induction of the ZnO nanomembrane, ZIF-67 would randomly nucleate in solution, rather than on the CFs. The ZnO nanomembrane, in contrast, improves the wettability and provides homogeneous nucleation sites on the CF to generate regular morphology and firm adhesion.

As shown in Fig. 3a–c and S4,† the obtained EDS results clearly demonstrate that Co, C, and N with high concentration are evenly distributed over the surface of the composite, implying the uniform growth of the ZIF-67 layer. The small amount of Zn should originate from the ZnO nanomembrane. The elemental composition and chemical states of Co-PSF were further investigated by XPS. The results confirm the presence of Co and N (Fig. 3d and e). The high-resolution Co $2p_{3/2}$ spectrum can be deconvoluted into 3 peaks at 781.5, 782.7, and 787.7 eV, corresponding to the Co^{3+}, Co^{2+}, and satellite species, respectively.[50] The coexisting Co^{2+} and Co^{3+} can be successively oxidized to Co^{4+} in the electrochemical reaction, which corresponds to the broad oxidation peak in the CV scans, as shown in Fig. 1e. In order to further study the structure of composites, the XRD patterns of Co-PSF, pristine CFs and ALD ZnO-CF are shown in Fig. 3f. The broad peak located at $2\theta = \sim 25^\circ$ for the CF is ascribed to the amorphous structure of carbon frameworks (plot: CF). After deposition of the ZnO nanomembrane, sharp diffraction peaks associated with the (100), (002), (101), (102), (110), and (103) lattice planes of wurtzite ZnO are observed (plot: ALD ZnO-CF), indicating the coexistence of the amorphous carbon and multi-crystal ZnO layer. After the induction process, almost all the ALD ZnO was converted into HDS, and then fully converted into the target ZIF-67 film. In Co-PSF, sharp peaks emerge, and all the peaks conformed well to the simulated pattern (Fig. 3f), which confirms the formation of the ZIF-67 layer. In addition, temperature is an important factor which highly affects the structural stability. TGA of Co-PSF is performed to estimate the thermostability of the composite. As shown in Fig. 3g, at a temperature higher than 300 °C, a gradual drop in mass can be seen, which is caused by oxidation degradation of organic linkers and carbon materials. This result proves the outstanding structural stability of Co-PSF for applications in a wide temperature range. The TGA results also indicate a high Co content in the composite, and this is beneficial for the subsequent electrochemical sensing. Here, in order to further investigate the pore structure of the resultant composites, the nitrogen adsorption–desorption isotherms and corresponding pore size distributions of Co-PSF and pristine CFs are shown in Fig. 3h and i. The CF exhibits a negligibly porous structure with a very low specific surface area of 0.3 $m^2\ g^{-1}$, while the Co-PSF shows a large surface area of 140 $m^2\ g^{-1}$. According to the nitrogen adsorption–desorption isotherms, both type I and type IV isotherms exist in Co-PSF (Fig. 3h), implying the existence of a hierarchically porous structure consisting of micropores and mesopores.[23,46] The obtained pore size distributions are also shown in Fig. 3i. Consistent with the isotherms, open mesopore peaks located at 3.82, 4.89, 7.79, and 17.45 nm can be clearly observed, indicating the formation of mesopores in the smart fiber. As a reference, the pore size distribution for CFs is also illustrated in Fig. 3i, and a completely different distribution is noticeable. In addition, the pore size distribution of ZIF-67 powder is shown in Fig. S5,† and only an apparent micropore peak centered at ~1.3 nm can be observed. Thus, the existence of mesopores in Co-PSF is attributed to the close stacking of MOF particles in the ZIF-67 layer. The unique pore structure of Co-PSF should promote the penetration of the electrolyte in electrochemical applications which will be discussed later.

3.2 Electrochemical behaviors

The detailed electrochemical behavior of Co-PSF is first studied in 0.1 M NaOH containing various concentrations of glucose by CV scanning in the range of −0.1 to 0.8 V. As shown in Fig. 4a, with the increase of the glucose concentration, the reduction peaks at ~0.4 and ~0.1 V and the oxidation peak at ~0.3 V are significantly strengthened, implying additional current provided by the oxidation of glucose. According to previous reports regarding the electrochemical oxidation reaction of Co-based materials,[38,51] Co^{2+} and Co^{3+} can be successively oxidized to Co^{4+} in alkaline aqueous solution, demonstrating a broad oxidation peak at ~0.3 V. Subsequently, glucose was oxidized by Co^{4+}, whereas Co^{4+} was reduced to Co^{3+} and Co^{3+} was reduced to Co^{2+}, which formed two reduction peaks at ~0.4 and ~0.1 V respectively.[38,51] The mechanism of glucose sensing is presumably based on the following equations:

$$[\mathrm{Co}^{2+}(\mathrm{MI})_2]_n + 2n\mathrm{OH}^- \rightarrow [\mathrm{Co}^{4+}(\mathrm{MI})_2(\mathrm{OH})]_n + 2n\mathrm{e}^-, \tag{3}$$

$$2[\mathrm{Co}^{4+}(\mathrm{MI})_2(\mathrm{OH})_2]_n + n\mathrm{C}_6\mathrm{H}_{12}\mathrm{O}_6 \rightarrow 2[\mathrm{Co}^{3+}(\mathrm{MI})_2(\mathrm{OH})]_n + n\mathrm{C}_6\mathrm{H}_{10}\mathrm{O}_6 + 2n\mathrm{H}_2\mathrm{O}, \tag{4}$$

$$[\mathrm{Co}^{3+}(\mathrm{MI})_2(\mathrm{OH})]_n + n\mathrm{e}^- \rightarrow [\mathrm{Co}^{2+}(\mathrm{MI})_2]_n + n\mathrm{H}_2\mathrm{O}. \tag{5}$$

Fig. S6† shows the influence of applied potential on the amperometric response of 1 mM glucose. Obviously, at 0.6 V, our smart fiber exhibits a remarkable and stable response. Therefore, the current–time (*I–t*) tests of the Co-PSF electrode are carried out at 0.6 V. As shown in Fig. S7a,† no obvious current response can be observed for CFs after successive addition of 1 mM glucose, indicating their poor electrochemical activity, while ZIF-67 exhibits very weak current responses due to the presence of catalytic Co-MI content (inset of Fig. S7a†). In contrast, distinct current steps are observed for Co-PSF, suggesting its strong electrocatalytic activity toward glucose oxidation. The specific current responses are recorded in Fig. S7b,† and one can see that the response current of Co-PSF (64 μA) is much larger than those of ZIF-67 (0.85 μA) and pristine CFs (0.106 μA). This phenomenon can be attributed to the interconnected catalytically active film with a hierarchically nanoporous structure. Compared with that of ZIF-67, the largely enhanced conductivity due to the contribution of CFs is also

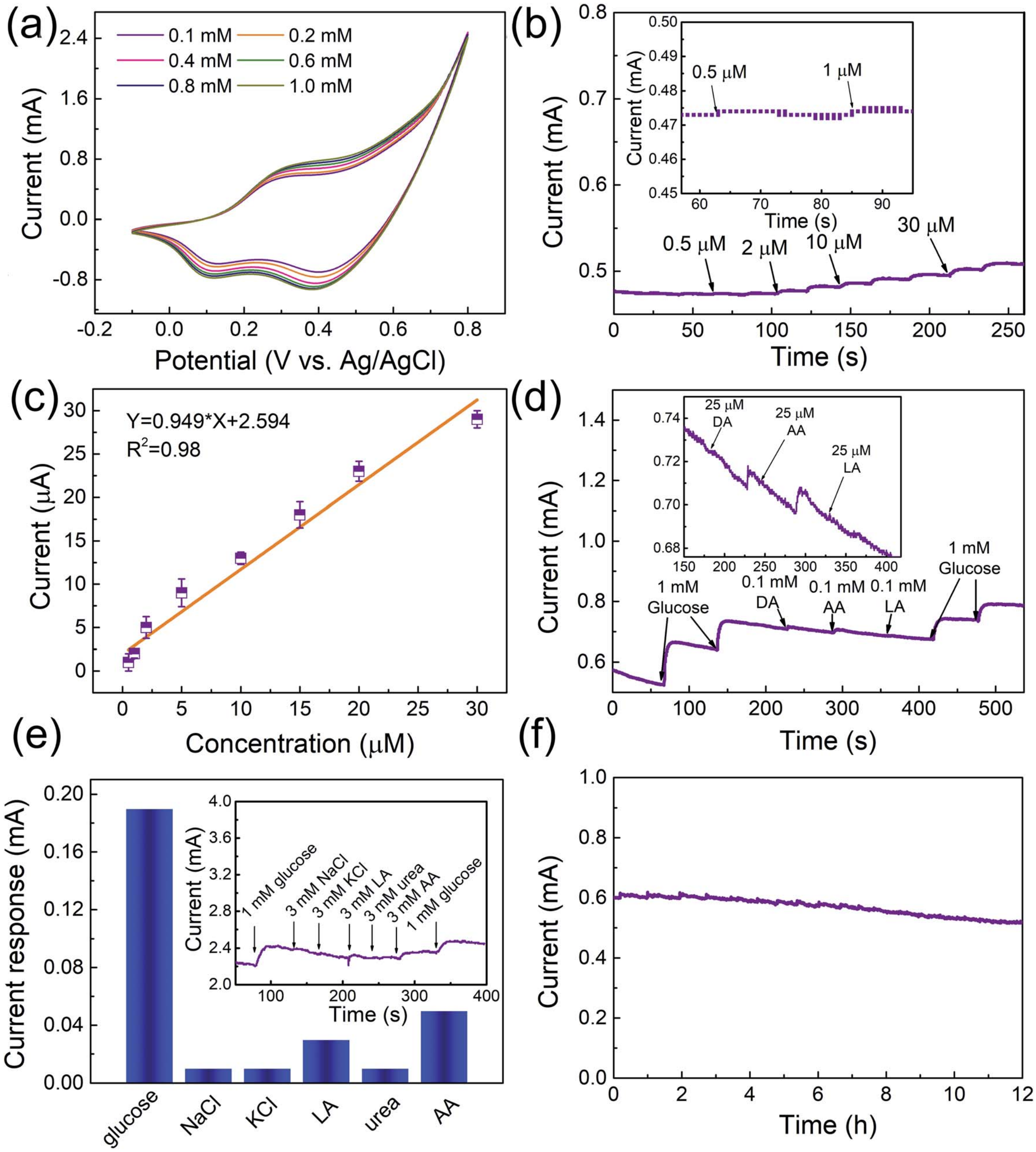

Fig. 4 (a) CV curves of Co-PSF within the potential range of −0.1 to 0.8 V in 0.1 M NaOH containing glucose with various concentrations at a scan rate of 20 mV s^{-1}. (b) *I*–*t* curve of Co-PSF with the successive addition of glucose in 0.1 M NaOH at a potential of 0.6 V. The inset shows the enlarged image. (c) Calibration plot derived from (b). (d) *I*–*t* curve of Co-PSF for the continuous addition of 1 mM glucose, 25 μM and 0.1 mM dopamine (DA), 25 μM and 0.1 mM ascorbic acid (AA), 25 μM and 0.1 mM lactic acid (LA), and 1 mM glucose at 0.6 V. The inset shows the enlarged image. (e) Current responses of 1 mM glucose, 3 mM NaCl, 3 mM KCl, 3 mM LA, 3 mM urea, and 3 mM AA at 0.6 V. The inset shows the *I*–*t* curve of Co-PSF with the successive addition of glucose and other interferents. (f) *I*–*t* curve of Co-PSF in 0.1 M NaOH with 1.0 mM glucose at 0.6 V.

beneficial to the electrochemical properties (Fig. S8†), leading to an apparent current response for glucose oxidation.

The non-enzymatic glucose sensing performance of Co-PSF was quantitatively evaluated. Fig. 4b illustrates the I-t curve of Co-PSF with the successive addition of glucose in 0.1 M NaOH at a potential of 0.6 V. With the addition of glucose, apparent and rapid current responses can be seen, and the corresponding calibration plot related to the concentration is shown in Fig. 4c. According to the calibration plot, the Co-PSF exhibits an ultra-high sensitivity of 4835 μA mM^{-1} cm^{-2} with a linear range of 0.0005–0.03 mM (linear regression equation: $Y = 0.949X + 2.594$; correlation coefficient (R^2): 0.98). In addition, the limit of detection (LOD) is calculated using the equation LOD $= 3\delta/S$, where δ is the standard deviation and S is the sensitivity. Here, a detection limit of 0.3 μM is obtained. Furthermore, we also evaluate the sensitivity at a high glucose concentration with CV tests. As shown in Fig. S9,† the calibration plot derived from the reduction peak at ~0.1 V exhibits a large slope, indicating the high sensitivity. Even at a high glucose concentration, the sensitivity of Co-PSF is as high as 1055 μA mM^{-1} cm^{-2} with

Table 1 Composite-based non-enzymatic glucose sensors and their sensing performances

Sample	Sensitivity μA mM^{-1} cm^{-2}	Linear range (mM)	LOD (μM)	Ref.
Co_3O_4/3D-rGO	112.16	Up to 1	0.157	53
NiO/rGO	666.71	0.005–4.2	5	54
NiO/Pt/ErGO	668.2	0.05–5.66	0.2	55
Pt/Ni nanowires	920	0.002–2	1.5	56
Ni–Ns–rGO hybrid	813	0.001–0.11	—	57
Graphene@ZIF-67	1521.1	0.001–0.8055	0.36	38
Mn_3O_4/N-doped rGO	1423.9	0.0025–0.5295	1	58
Ni/ATPa/rGOb	1414.4	0.001–0.71	0.37	59
CuO NS/CC	4901.96	Up to 1	1	60
CuO NW/CC	2973.2	Up to 1.12	1	60
CuO NPs/CNTs on Ta foil	2596	Up to 1.2	0.2	61
Ni–Cu/TiO_2NTs	1590	Up to 3.2	5	62
Co_3O_4 microspheres	1440	0.005–12	0.15	63
CuO NWs/Cu foil	1420.3	Up to 2.05	5.1	64
Co-PSF	**4835**	**0.0005–0.03**	**0.3**	**This work**

a linear range of 0.1–1 mM, where the linear regression equation is $Y = 0.2072X + 0.5755$ and correlation coefficient (R^2) is 0.99. We should stress that these values can compare favorably with those of plenty of other electrochemical glucose sensors in previous reports.[38,53–64] The detailed comparison of the sensing performance is summarized in Table 1. We further investigated the electrochemical properties of Co-PSF with additional characterization. The CV curves of Co-PSF in 0.1 M NaOH at various scan rates are depicted in Fig. S10a.† The oxidation peak shows a slightly positive shift and the reduction peaks shift negatively with the increase of the scan rate. And both the oxidation and the reduction peaks become vague at high scan rates. This phenomenon can be attributed to the insufficient electrochemical reaction.[38] Fig. S10b† shows that the currents of both the oxidation and reduction peaks increase linearly with the square root of the scan rates in the range of 10–80 mV s^{-1}. This good linear relationship indicates a diffusion-controlled electrochemical process.[52] The anti-interference ability is another important property to evaluate the sensing performance. Fig. 4d shows the *I–t* curves of Co-PSF for the continuous addition of 1 mM glucose, 25 μM and 0.1 mM dopamine (DA), 25 μM and 0.1 mM ascorbic acid (AA), 25 μM and 0.1 mM lactic acid (LA), and 1 mM glucose. The *I–t* curve demonstrates that DA, AA, and LA produce little current response compared with glucose, demonstrating the good anti-interference ability. In addition, to verify the practicality of the Co-PSF sensor, selectivity and stability are evaluated. As shown in the inset of Fig. 4e, the *I–t* curve of Co-PSF with consecutive introduction of 1 mM glucose and 3 mM interferents (*e.g.*, NaCl, KCl, LA, urea, and AA) illustrates the significant current response with the addition of target glucose. Except for a tiny fluctuation due to vibration when 3 mM LA is added, one can see only negligible response when adding a series of interferents, indicating the good selectivity of Co-PSF to the target molecule. The current responses towards these molecules are quantitatively demonstrated in Fig. 4e. Negligible current responses from interferents are observed when the concentrations of interferents are three times higher than that of target glucose, implying the great potential in practical applications. The electrochemical stability of Co-PSF is evaluated in 0.1 M NaOH containing 1 mM glucose at 0.6 V. As shown in Fig. 4f, the composite exhibits a current response at ∼0.6 mA with great stability within 12 h. The composition and morphology of the Co-PSF after the 12 h *I–t* test were characterized with SEM, EDS, and XRD, and the results are shown in Fig. S11–S13.† No obvious morphological and compositional change can be seen (see also Fig. 3). No peeling off of the ZIF-67 layer can be observed, indicating firm attachment of the active layer due to the ALD induction. In addition, in the XRD pattern of Co-PSF after the 12 h test (Fig. S13†), all the sharp peaks can be associated with ZIF-67, indicating the preservation of the ZIF-67 layer. All these characterization results further prove the good stability of the Co-PSF composite even after long term glucose sensing.

The outstanding sensing performance of the current Co-PSF can be attributed to the following factors. Firstly, as mentioned above, the oxide nanomembrane induced assembly of the MOF film results in firm attachment and homogeneous coating, and the MOF particles stack closely to form the dense functional film. This should greatly improve the structural stability. Secondly, the hierarchically nanoporous structure including mesopores and micropores leads to the exposure of more active sites and penetration of the electrolyte. Thirdly, multiple conductive pathways in accordance with the conductive CFs in the composite promote the electron transfer and further enhance the sensing performance.

3.3 Flexible performance

Due to the outstanding flexibility of our smart fiber, we further spin the fiber into a functional textile to evaluate the electrochemical performance under repeated bending conditions. As shown in Fig. 5a, the smart textile indeed demonstrates excellent flexibility. We further test the sensing performance of the flexible textile. In our experiment, the smart textile was fixed using a conductive clip, bent to 180°, and then unfolded to restore the original geometry. Fig. 5b shows the CV curves of the smart textile before and after bending, and a slight change can be observed, proving that the corresponding sensing device can sense target glucose even under severe deformation. Fig. 5c exhibits the CV curves of the smart textile after repeated

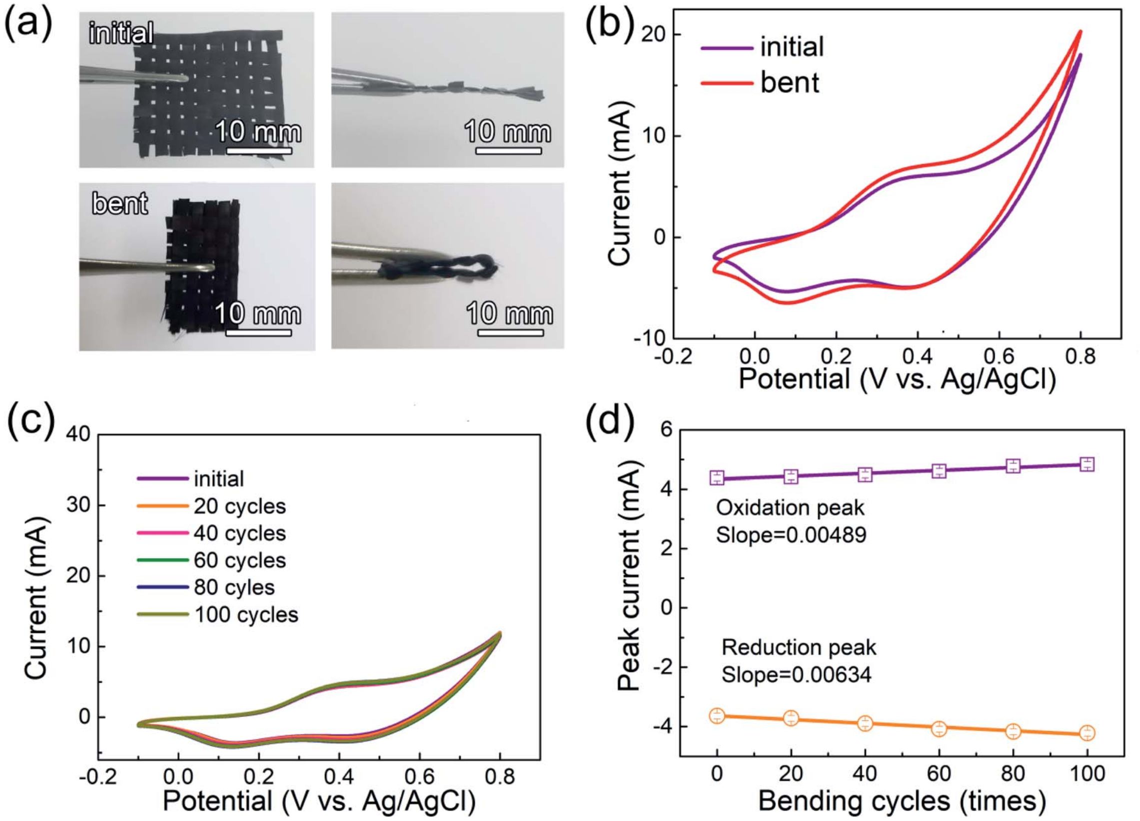

Fig. 5 (a) The photographs (top and side views) of the smart textile before and after 180° bending. (b) CV curves of the smart textile before and after 180° bending. (c) CV curves of the smart textile over up to 100 bending cycles in 0.1 M NaOH containing 1 mM glucose. (d) The peak currents as a function of bending cycles.

bending cycles (up to 100 cycles), and the oxidation peak current and reduction peak current as a function of the number of bending cycles are shown in Fig. 5d. These results further validate the stability of the sensing performance. The outstanding flexibility of Co-PSF and the corresponding smart textile can be attributed to several reasons. The pristine CF, as the supporting substrate, possesses natural flexibility. The assembly of the functional layer by ALD induction provides intimate adhesion and the stable interface hinders the peeling off of the functional layer under deformation. Besides, the hierarchically porous structure provides vacancies in the functional layer, which enables the functional layer to accommodate some of the deformations. The flexibility of Co-PSF and the corresponding textile thus enables efficient sensing when attached to human skin, and the high deformation tolerance enhances the potential for practical uses like in diagnosis and biological monitoring. We therefore provide a strategy of synthesizing functional smart fibers with the potential for structural innovation as well as practical applications in the fields of smart textiles, smart cloth, and wearable electronics.

4 Conclusion

The Co-PSF composite is fabricated by HDS salt conversion *via* ALD ZnO nanomembrane induction. The resultant smart fiber shows a unique structure, where a homogeneous functional film is assembled and attaches firmly to the conductive flexible CF. The composite with a hierarchically nanoporous structure has a large surface area and good flexibility and can be woven into a smart textile to achieve flexible glucose sensing. The advanced composite structure leads to excellent sensing performance like an ultrahigh sensitivity of 4835 μA mM^{-1} cm^{-2} in the linear range of 0.0005–0.03 mM and a limit of detection of 0.3 μM. In addition, the resultant composite with outstanding flexible properties can sense glucose during large and repeated deformation cycles. This study therefore provides a strategy of fabricating smart fibers as well as smart cloth applied in advanced biomedicine and wearable electronics-related fields.

Conflicts of interest

The authors declare no competing financial interest.

Acknowledgements

This work was supported by the National Natural Science Foundation of China (No. 51961145108 and 61975035), the Science and Technology Commission of Shanghai Municipality (No. 19XD1400600 and 17JC1401700), and the National Key Research and Development Project of China (No. 2017YFE0112000).

Notes and references

1 K. Furuyama, S. Chera, L. V. Gurp, D. Oropeza, L. Ghila, N. Damond, H. Vethe, J. A. Paulo, A. M. Joosten, T. Berney, D. Bosco, C. Dorrell, M. Grompe, H. Raeder, B. O. Roep, F. Thorel and P. L. Herrera, *Nature*, 2019, **567**, 43–48.

2 Y. Oh, J. S. Y. Lai, H. J. Mills, B. H. Erdjument, B. Giammarinaro, K. Saadipour, J. G. Wang, F. Abu, T. A. Neubert and G. S. B. Suh, *Nature*, 2019, **574**, 559–564.

3 W. V. Tamborlane, R. W. Beck, B. W. Bode, B. Buckingham, H. P. Chase, R. Clemons, S. R. Fiallo, L. A. Fox, L. K. Gilliam, I. B. Hirsch, E. S. Huang, C. Kollman, A. J. Kowalski, L. Laffel, J. M. Lawrence, J. Lee, N. Mauras, M. O'Grady, K. J. Ruedy, M. Tansey, E. Tsalikian, S. Weinzimer, D. M. Wilson, H. Wolpert, T. Wysocki and D. Xing, *N. Engl. J. Med.*, 2008, **359**, 1464–1465.

4 W. Gao, S. Emaminejad, H. Y. Y. Nyein, S. Challa, K. Chen, A. Peck, H. M. Fahad, H. Ota, H. Shiraki, D. Kiriya, D. H. Lien, G. A. Brooks, R. W. Davis and A. Javey, *Nature*, 2016, **529**, 509–514.

5 D. Holmes, *Nat. Rev. Endocrinol.*, 2016, **12**, 247.

6 Y. J. Hong, H. Lee, J. Kim, M. Lee, H. J. Choi, T. Hyeon and D. H. Kim, *Adv. Funct. Mater.*, 2018, **28**, 1805754.

7 G. Xiao, J. He, X. Chen, Y. Qiao, F. Wang, Q. Xia, L. Yu and Z. Lu, *Cellulose*, 2019, **26**, 4553–4562.

8 W. Y. He, C. Y. Wang, H. M. Wang, M. Q. Jian, W. D. Lu, X. P. Liang, X. Zhang, F. C. Yang and Y. Y. Zhang, *Sci. Adv.*, 2019, **5**, 1–8.

9 J. Kim, A. S. Campbell, B. E. F. de Avila and J. Wang, *Nat. Biotechnol.*, 2019, **37**, 389–406.

10 Y. Li, M. W. Xie, X. P. Zhang, Q. Liu, D. M. Lin, C. H. Xu, F. Y. Xie and X. P. Sun, *Sens. Actuators, B*, 2019, **278**, 126–132.

11 R. Bruch, J. Baaske, C. Chatelle, M. Meirich, S. Madlener, W. Weber, C. Dincer and G. A. Urban, *Adv. Mater.*, 2019, **31**, 1905311.

12 Y. Yu, H. Y. Y. Nyein, W. Gao and A. Javey, *Adv. Mater.*, 2020, **32**, 1902083.

13 G. Y. Li, Z. H. Li, X. Xiao, Y. L. An, W. Wang and Z. Q. Hu, *J. Mater. Chem. A*, 2019, **7**, 11077–11085.

14 N. K. Navani and Y. Li, *Curr. Opin. Chem. Biol.*, 2006, **10**, 272–281.

15 J. O. Shimazaki, H. Yoshida and K. Sode, *Bioelectrochemistry*, 2020, **132**, 107414.

16 N. Saravanan and A. S. Kumar, *Methods Enzymol.*, 2020, **630**, 249–262.

17 W. W. Chen, W. S. Yang, Y. L. Lu, W. J. Zhu and X. Chen, *Anal. Methods*, 2017, **9**, 3213–3220.

18 P. Cheng, C. Wang, Y. V. Kaneti, M. Eguchi, J. Lin, Y. Yamauchi and J. Na, *Langmuir*, 2020, **36**, 4231–4249.

19 W. R. Cheng, X. Zhao, H. Su, F. M. Tang, W. Che, H. Zhang and Q. H. Liu, *Nat. Energy*, 2019, **4**, 115–122.

20 S. Dang, Q. L. Zhu and Q. Xu, *Nat. Rev. Mater.*, 2018, **3**, 17075.

21 L. Pan, G. Liu, W. X. Shi, J. Shang, W. R. Leow, Y. Q. Liu, Y. Jiang, S. Z. Li, X. D. Chen and R. W. Li, *Nat. Commun.*, 2018, **9**, 3813.

22 X. T. Xu, T. Yang, Q. W. Zhang, W. Xia, Z. B. Ding, K. Eid, A. M. Abdullah, M. S. A. Hossain, S. H. Zhang, J. Tang, L. K. Pan and Y. Yamauchi, *Chem. Eng. J.*, 2020, **390**, 124493.

23 Z. Zhao, S. L. Liu, J. X. Zhu, J. S. Xu, L. Li, Z. Q. Huang, C. Zhang and T. X. Liu, *ACS Appl. Mater. Interfaces*, 2018, **10**, 19871–19880.

24 S. Liu, J. L. Bai, Y. P. Huo, B. A. Ning, Y. Peng, S. Li, D. P. Han, W. J. Kang and Z. X. Gao, *Biosens. Bioelectron.*, 2020, **149**, 111801.

25 D. Uzak, A. Atiroğlu, V. Atiroğlu, B. Çakıroğlu and M. Özacar, *Electroanalysis*, 2020, **32**, 510–519.

26 G. Gumilar, Y. V. Kaneti, J. Henzie, S. Chatterjee, J. Na, B. Yuliarto, N. Nugraha, A. Patah, A. Bhaumik and Y. Yamauchi, *Chem. Sci.*, 2020, **11**, 3644–3655.

27 B. B. Liu, X. Y. Wang, H. Q. Liu, Y. Y. Zhai, L. Li and H. R. Wen, *Anal. Chim. Acta*, 2020, **1122**, 9–19.

28 Z. Xue, L. Jia, R. R. Zhu, L. Du and Q. H. Zhao, *J. Electroanal. Chem.*, 2020, **858**, 113783.

29 S. H. Zhang, J. Y. Wang, N. L. Torad, W. Xia, M. A. Aslam, Y. V. Kaneti, Z. F. Hou, Z. J. Ding, B. Da, A. Fatehmulla, A. M. Aldhafiri, W. A. Farooq, J. Tang, Y. Bando and Y. Yamauchi, *Small*, 2020, **16**, 1901718.

30 Z. L. Chen, Y. Ha, H. X. Jia, X. X. Yan, M. Chen, M. Liu and R. B. Wu, *Adv. Energy Mater.*, 2019, **9**, 1803918.

31 Z. L. Chen, R. B. Wu, Y. Liu, Y. Ha, Y. H. Guo, D. L. Sun, M. Liu and F. Fang, *Adv. Mater.*, 2018, **30**, 1802011.

32 X. Zhang, K. Wan, P. Subramanian, M. W. Xu, J. S. Luo and J. Fransaer, *J. Mater. Chem. A*, 2020, **8**, 7569–7587.

33 Z. Y. Wang, T. Liu, M. Asif, Y. Yu, W. Wang, H. T. Wang, F. Xiao and H. F. Liu, *ACS Appl. Mater. Interfaces*, 2018, **10**, 27936–27946.

34 H. B. Wu and L. X. Wen, *Sci. Adv.*, 2017, **3**, 12.

35 P. Falcaro, R. Ricco, C. M. Doherty, K. Liang, A. J. Hill and M. J. Styles, *Chem. Soc. Rev.*, 2014, **43**, 5513.

36 M. Z. Iqbal, M. M. Faisal, S. R. Ali, S. Farid and A. M. Afzal, *Electrochim. Acta*, 2020, **346**, 136039.

37 H. L. Zhu and D. X. Liu, *J. Mater. Chem. A*, 2019, **7**, 21004–21035.

38 X. R. Chen, D. Lau, G. J. Cao, Y. Tang and C. Wu, *ACS Appl. Mater. Interfaces*, 2019, **11**, 9374–9384.

39 X. G. Feng, S. R. Lin, M. Li, X. J. Bo and L. P. Guo, *Anal. Chim. Acta*, 2017, **984**, 96–106.

40 Q. G. Han, W. Q. Zhang, Z. W. Han, S. C. Niu, J. Q. Zhang, F. X. Wang, X. Li, D. Geng and G. Yu, *Ionics*, 2019, **25**, 5333–5340.

41 W. M. Zhang, X. Y. Yao, S. N. Zhou, X. W. Li, L. Li, Z. Yu and L. Gu, *Small*, 2018, **14**, 1800423.

42 C. C. Sun, Q. C. Dong, J. Yang, Z. Y. Dai, J. J. Lin, P. Chen, W. Huang and X. C. Dong, *Nano Res.*, 2016, **9**, 2234–2243.

43 T. Zhou, J. D. Shen, Z. S. Wang, J. Liu, R. Z. Hu, L. Z. Ouyang, Y. Z. Feng, H. Liu, Y. Yu and M. Zhu, *Adv. Funct. Mater.*, 2020, **30**, 1909159.

44 J. Hou, P. D. Sutrisna, T. Wang, S. Gao, Q. Li, C. Zhou, S. Sun, H. C. Yang, F. Wei, M. T. Ruggiero, J. A. Zeitler, A. K. Cheetham, K. Liang and V. Chen, *ACS Appl. Mater. Interfaces*, 2019, **11**, 5570–5577.

45 Z. Zhao, Y. Kong, C. Liu, J. R. Liu, Z. J. Wang, G. F. Zheng, G. S. Huang and Y. F. Mei, *J. Materiomics*, 2020, **6**, 209–215.

46 Z. Zhao, Z. W. Zhang, Y. T. Zhao, J. R. Liu, C. Liu, Z. J. Wang, G. F. Zheng, G. S. Huang and Y. F. Mei, *Adv. Funct. Mater.*, 2019, **29**, 1906365.

47 F. Rezaei, R. Yunus, N. A. Ibrahim and E. S. Mahdi, *Polym.-Plast. Technol. Eng.*, 2008, **47**, 351–357.

48 Z. Zhao, Y. Kong, Z. W. Zhang, G. S. Huang and Y. F. Mei, *J. Mater. Res.*, 2020, **35**, 701–719.

49 J. J. Zhao, W. T. Nunn, P. C. Lemaire, Y. Lin, M. D. Dickey, C. J. Oldham, H. J. Walls, G. W. Peterson, M. D. Losego and G. N. Parsons, *J. Am. Chem. Soc.*, 2015, **137**, 13756–13759.

50 Y. Y. Wen, Z. T. Wei, C. Ma, X. F. Xing, Z. Li and D. Luo, *Nanomaterials*, 2019, **9**, 775.

51 Y. Ding, Y. Wang, L. A. Su, M. Bellagamba, H. Zhang and Y. Lei, *Biosens. Bioelectron.*, 2010, **26**, 542–548.

52 Y. X. Zhang, J. Y. Xu, J. F. Xia, F. F. Zhang and Z. H. Wang, *ACS Appl. Mater. Interfaces*, 2018, **10**, 39151–39160.

53 L. Bao, T. Li, S. Chen, C. Peng, L. Li, Q. Xu, Y. S. Chen, E. Ou and W. J. Xu, *Small*, 2017, **13**, 1602077.

54 G. S. Zeng, W. P. Li, S. Q. Ci, J. C. Jia and Z. H. Wen, *Sci. Rep.*, 2016, **6**, 36454.

55 M. Li, X. J. Bo, Z. C. Mu, Y. F. Zhang and L. P. Guo, *Sens. Actuators, B*, 2014, **192**, 261–268.

56 S. S. Mahshid, S. Mahshid, A. Dolati, M. Ghorbani, L. Yang, S. Luo and Q. Cai, *Electrochim. Acta*, 2011, **58**, 551–555.

57 T. Choi, S. H. Kim, C. W. Lee, H. Kim, S. K. Choi, S. H. Kim, E. Kim, J. Park and H. Kim, *Biosens. Bioelectron.*, 2015, **63**, 325–330.

58 S. L. Yang, G. Li, G. F. Wang, J. H. Zhao, X. H. Gao and L. B. Qu, *Sens. Actuators, B*, 2015, **221**, 172–178.

59 Z. X. Shen, W. Y. Gao, P. Li, X. F. Wang, Q. Zheng, H. Wu, Y. H. Ma, W. J. Guan, S. M. Wu, Y. Yu and K. J. Ding, *Talanta*, 2016, **159**, 194–199.

60 Y. Zhong, T. L. Shi, Z. L. Liu, S. Y. Cheng, Y. Y. Huang, X. X. Tao, G. L. Liao and Z. R. Tang, *Sens. Actuators, B*, 2016, **236**, 326–333.

61 L. C. Jiang and W. D. Zhang, *Biosens. Bioelectron.*, 2010, **25**, 1402–1407.

62 X. L. Li, J. Y. Yao, F. L. Liu, H. C. He, M. Zhou, N. Mao, P. Xiao and Y. H. Zhang, *Sens. Actuators, B*, 2013, **181**, 501–508.

63 C. Y. Guo, X. Zhang, H. H. Huo, C. L. Xu and X. Han, *Analyst*, 2013, **138**, 6727–6731.

64 Y. C. Li, M. G. Zhao, J. Chen, S. S. Fan, J. J. Liang, L. J. Ding and S. G. Chen, *Sens. Actuators, B*, 2016, **232**, 750–757.